ELSEVIER

Contents lists available at SciVerse ScienceDirect

# Chemical Engineering Journal

journal homepage: www.elsevier.com/locate/cej

Chemical Engineering Journal

# Zero-valent iron (ZVI) Fenton oxidation of reactive dye wastewater under UV-C and solar irradiation

Ivana Grčić\*, Sanja Papić, Krunoslav Žižek, Natalija Koprivanac

University of Zagreb, Faculty of Chemical Engineering and Technology, Marulićev trg 19, 10000 Zagreb, Croatia

#### HIGHLIGHTS

- ▶ Photo-Fenton catalysis with immobilized ZVI.
- ▶ Reactors with maximized ZVI surface area exposed to irradiation.
- ▶ Optimization via mixture design.
- ► Empirical expression for the generation of Fe<sup>2+</sup> from ZVI surface upon corrosion.
- ▶ Developed model for the homogeneous catalysis.

#### ARTICLE INFO

Article history:
Received 16 December 2011
Received in revised form 26 April 2012
Accepted 28 April 2012
Available online 7 May 2012

Keywords: Zero-valent iron (ZVI) Photo-Fenton Solar Fenton Mixture design Catalysis Kinetic modeling

#### ABSTRACT

In the frame of this work, photo-Fenton processes using the zero-valent iron (ZVI) as a catalyst have been applied for mineralization and decolourization of the model wastewater containing reactive azo dye, C.I. Reactive Black 1 (RB1). Experiments were performed in the enhanced configuration of laboratory cylindrical batch photoreactor under UV-C irradiation (CBPR) and the boat-shaped flow reactor (BSFR) in total recirculation mode, exposed to direct sunlight, both with the immobilized iron.

In the first part of the study, optimization of UV-C/ZVI-Fenton process has been performed using the concept of experimental mixture design, whereas Fenton reagent composition (ZVI and  $H_2O_2$ ) and pH condition were treated as a three-component mixture. Due to the strict boundaries and constraints of mixture design, a single point in the design space emerged upon each optimization cycle.

Corresponding kinetics was studied at optimal conditions. Two approaches has been compared; in the first approach a heterogeneous catalytic pathway has been adopted, while the second approach assumed the pure homogeneous catalysis, exploring the crucial role of the Fe(II) ions in the bulk solution due to its leaching from the ZVI surface. Corrosion of ZVI surface was examined by the means of material characterization and Fe(II) leaching.

© 2012 Elsevier B.V. All rights reserved.

# 1. Introduction

Advanced oxidation processes (AOPs) have been proven particularly effective for the treatment of a wide variety of wastewater containing recalcitrant organic pollutants, including the most of the synthetic dyestuffs, due to the generation of free hydroxyl radicals ('OH), which are very reactive due to high oxidation potential [1]. The production of hydroxyl radicals is the most enhanced by the reaction of ferrous ion (Fe<sup>2+</sup>) as a catalyst and  $\rm H_2O_2$  as an oxidant in the Fenton reaction cycle [2]. Numerous studies on the treatment of textile dye effluents include Fenton and photo-Fenton processes [3–10]. Photo-Fenton processes demonstrated its great capability for color removal and pollutant degradation through

the involvement of high valence Fe-intermediates responsible for the direct attack to organic matter. Also, photo-Fenton processes are a potential cost-reduced advanced oxidation process that can be run under solar irradiation [11].

Zero-valent iron appears as an effective catalyst for wastewater treatment in Fenton type processes [12–16]. There are different ways to produce Fe(II).

$$Fe^{0} \overset{H_{2}O_{2},H^{+}}{\to} Fe^{2+} + 2e^{-} \tag{1}$$

$$Fe^0 + h\nu \rightarrow Fe^{2+} + 2e^-(< 400 \text{ nm})$$
 (2)

$$Fe^0 \stackrel{O_2}{\to} Fe^{2+} + 2e^- \eqno(3)$$

$$2Fe^0 + O_2 + 2H_2O \rightarrow 2Fe^{2+} + 4OH^- \tag{4}$$

<sup>\*</sup> Corresponding author. Tel.: +385 14597 123; fax: +385 14597 142. *E-mail address*: igrcic@fkit.hr (I. Grčić).

$$2Fe^{0} + O_{2} + 4H^{+} \rightarrow 2Fe^{2+} + 2H_{2}O \tag{5}$$

$$Fe^0 + O_2 + 2H^+ \rightarrow Fe^{2+} + H_2O_2$$
 (6)

Applied irradiation causes the cleavage of iron complexes (-hydro-xy, -oxalate and similar) present in the system [2,17]. In addition,  $Fe^{2+}$  as a free cation and additional portion of OH radicals are formed, Eqs. (7)–(9). Note that  $Fe^{3+}$ –OC refers to ferric complexes with corresponding organic ligand.

$$[Fe(OH)]^{2+} + h\nu \rightarrow Fe^{2+} + OH$$
 (7)

$$Fe^{3+} + H_2O + h\nu \rightarrow Fe^{2+} + H^+ + OH$$
 (8)

$$Fe^{3+} - OC + h\nu \rightarrow Fe^{2+} + organic radical$$
 (9)

Adsorbed  $O_2$  on the Fe surface contribute to the generation of  $H_2O_2$  in situ [12–15].

$$O_{2ads} + e^- \rightarrow O_2^{--} + HO_2^{--}$$
 (10)

$$HO_{2}^{-}(+O_{2}^{-}) + H^{+} \rightarrow H_{2}O_{2} + H_{2}(in \ situ)$$
 (11)

Perhydroxyl radical ( $HO_2$ ), a precursor towards  $H_2O_2$ , is formed from the photolysis of water [12].

$$2H_2O + hv \rightarrow HO_2 + 3H^+(< 698 \text{ nm})$$
 (12)

Finally, 'OH radicals are generated.

$$Fe^{2+} + H_2O_2 \rightarrow Fe^{3+} + OH + OH^-$$
 (13)

Recent studies point out the reductive nature of ZVI towards azo dyes due to the reductive cleavage of azo bond at different pH values of the system [18–20].

Application of ZVI-Fenton and photo-Fenton processes for treatment of simulated textile wastewaters containing azo dyes has already been thoroughly investigated [1,21,22]. However, the novelties presented in this work refer to the application of two reactor types with maximized ZVI surface area exposed to irradiation and optimization of ZVI-photo-Fenton process via mixture design. The applied optimization methodology entails the constraints that narrow the optimization possibilities thus resulting with the single optimal point. Mineralization and decolourization of the RB1 aqueous solution (hereafter: oxidation) have been successfully carried out by the simultaneous use of Fenton reagent (ZVI and  $H_2O_2$ ) and UV-C or solar irradiation. Oxidation kinetics was

determined in terms of total organic content reduction (hereafter: OC oxidation) and dye molecule breakdown (hereafter: RB1 oxidation). Heterogeneous and homogeneous kinetic approaches for description of ZVI-photo-Fenton catalysis were compared. Formal kinetic scheme for the homogenous Fenton has been adopted from the recent publication [23], resulting with the simple model (hereafter: homogeneous kinetic model) for OC and RB1 oxidation kinetics. In addition, a complex model including  $\rm H_2O_2$  photolysis and  $\rm ^{\circ}OH$  radicals recombination has been developed. It has been shown that initial concentration of Fe(II) ions released from corroded ZVI surface plays a crucial role for OC and RB1 oxidation. Influence of applied irradiation has been discussed. Solar light irradiation was found to be highly effective, opening the possibility of low cost applications of solar-ZVI catalysis.

# 2. Methodology

# 2.1. Reagents and auxiliary chemicals

All reagents used in this work were analytical grade and used without any further purification. Zero-valent iron (ZVI) and hydrogen peroxide ( $H_2O_2$ , 30%) were supplied by Kemika, Croatia. Synthetic dye, C.I. Reactive Black 1 (RB1) (Table 1) was obtained from Ciba. Other chemicals used in different aspects of experimental work were as follows; potassium thiocyanate (KSCN), 1,10-phenantroline, potassium iodide (KI), potassium iodate (KIO<sub>3</sub>), sodium tetraborate (Na<sub>2</sub>B<sub>4</sub>O<sub>7</sub>·6H<sub>2</sub>O), sodium acetate (NaCH<sub>3</sub>COO) and glacial acetic acid were supplied by Kemika. Hydrochloric acid was supplied by Riedel de-Haën. Ammonium metavanadate (NH<sub>4</sub>VO<sub>3</sub>) was obtained from Sigma–Aldrich. Sulphuric acid (1 mol L<sup>-1</sup>) and sodium hydroxide (1 mol L<sup>-1</sup>) were used for the pH adjustment, all supplied by Kemika.

#### 2.2. Photoreactors

Novel reactor configurations have been presented (Figs. 1 and 2). Experiments were performed in a cylindrical laboratory batch reactor made from Pyrex glass with the immobilized iron using the flexible magnetic stripes, **CBPR** (Fig. 1), with the working volume of 125 mL and constant magnetic stirring (400 rpm). Low-pressure mercury lamp (PenRay 90-0012-01, UVP) with the primary emission output at 254 nm was used as the source of UV-C irradiation. UV lamp was placed axial in a quartz tube inside

**Table 1**Structure, absorption characteristics and photolytic data of C.I. Reactive Black 1.

Structure	Absorption characteristics and photolysis rates <sup>*</sup>
NaO <sub>3</sub> S Nh Nh Nh NaO <sub>3</sub> S Nh Nh Nh Nh	$\lambda_{\text{max-vis}} = 590 \text{ nm}$ $\epsilon_{590\text{nm}} = 7013.2 \text{ L mol}^{-1} \text{ cm}^{-1}$ $\epsilon_{\text{solar,average}} = 4519.4 \text{ L mol}^{-1} \text{ cm}^{-1}$ $r_{\text{UV-}}$ $\epsilon_{\text{solar,average}} = 2.8 \times 10^{-9} \text{ mol L}^{-1} \text{ s}^{-1}$ $\epsilon_{254\text{nm}} = 9520.8 \text{ L mol}^{-1} \text{ cm}^{-1}$ $\epsilon_{\text{UV-254nm}} = 1.6 \times 10^{-9} \text{ mol L}^{-1} \text{ s}^{-1}$
M =Cr, Co (1:1)	
Molar mass = $710.355 \mathrm{g}\mathrm{mol}^{-1}$	

<sup>\*</sup> Photolysis rate are calculated according to the control experiments (see Section 2.4.1).

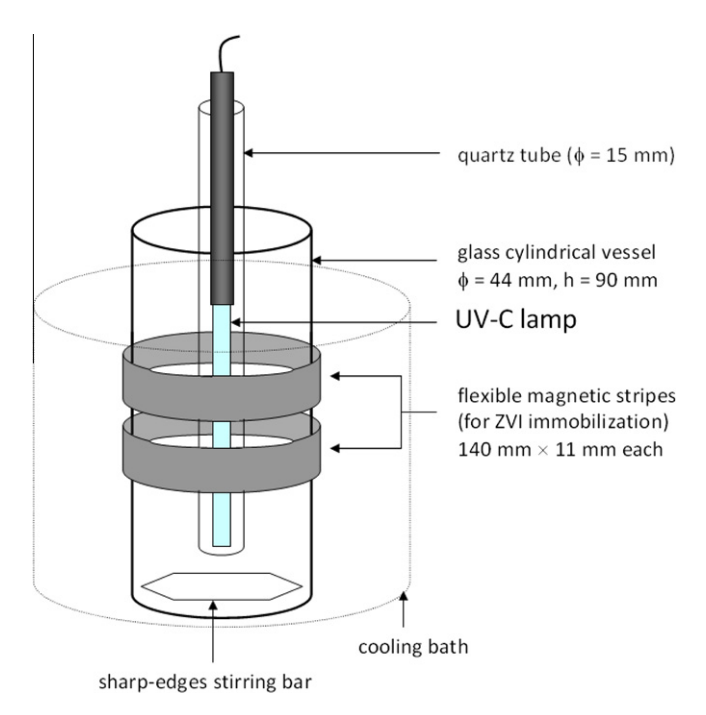
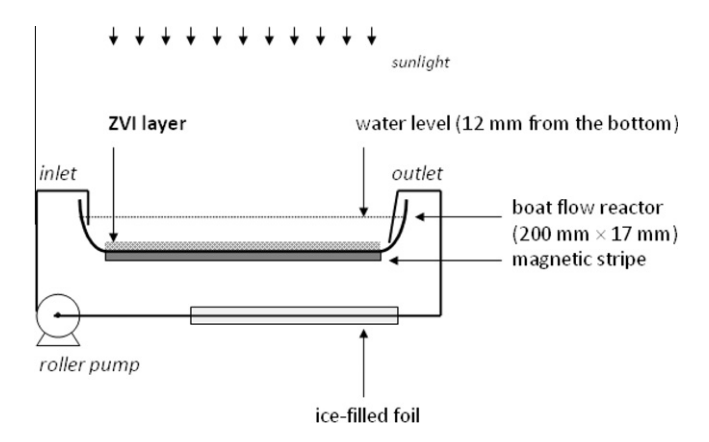


Fig. 1. Schematics and geometric characteristics of a laboratory batch reactor (CBPR)



**Fig. 2.** Schematics and geometric characteristics of boat-shaped solar reactor operated in total recirculation mode (BFSR).

the reactor. The temperature of reaction mixture was kept at 28  $\pm\,2\,^{\circ}\text{C}.$ 

Experiments involving solar irradiation were performed in the boat-shaped flow solar reactor with immobilized iron powder at the bottom, **BFSR** (Fig. 2), in the total recirculation mode (Masterflex Easyload 7518 peristaltic pump with silicon tubings, flow rate 80 mL min<sup>-1</sup>) with a total volume of 100 mL. Due the continuous flow through cooled tubing, temperature did not exceed 31 °C.

## 2.3. Mixture design

The simplex lattice mixture design was used to find an optimal composition of the Fenton reagent. Having in mind the main characteristic of a mixture design whereas single components are expressed as the fraction of the total amount and their sum must add up to 1 (or 100%) [24], concentration of the observed components (ZVI,  $\rm H_2O_2$ ) and pH value were translated into the coded composition, ranging from 0 to 1 (Table 2). The experimental plan includes the 14 compositions of the mixture with the different

**Table 2**Coded mixture components and actual values of the reagent dosage and pH.

Mixture component	Parameter	Coded composition	Actual process conditions
Α	Fe <sup>0</sup>	0 – 1	0.1 – 0.6 g
В	$H_2O_2$	0 - 1	$0 - 0.1 \text{ mol } L^{-1}$
С	pН	0 - 1	2 - 7

**Table 3**Coded mixture composition and observed responses in UV-C/ZVI-Fenton process.

Experimental	Code	ed con	nposit	ion		Responses	_
run #	Fe <sup>0</sup>	H <sub>2</sub> O <sub>2</sub>	pН	<i>X</i> <sub>TOC</sub> (%)	$X_{colour}$ (%)	[Fe <sup>2+</sup> ] (mmol L <sup>-1</sup> )	[Fe <sup>3+</sup> ] (mmol L <sup>-1</sup> )
1	1.00	0.00	0.00	11.16	49.52	2.550	0.249
2	0.67	0.17	0.17	60.12	85.79	0.128	1.378
3	0.50	0.50	0.00	64.31	98.44	0.191	3.601
4	0.00	1.00	0.00	48.51	99.10	0.389	3.231
5	0.00	1.00	0.00	54.80	98.91	0.253	2.006
6	0.00	0.00	1.00	0.16	38.15	0.027	0.163
7	0.33	0.33	0.33	64.46	99.42	0.070	0.175
8	0.17	0.17	0.67	14.23	90.93	0.100	0.025
9	0.50	0.00	0.50	4.83	29.09	0.175	0.135
10	0.00	0.50	0.50	22.66	96.13	0.090	0.052
11	0.00	0.00	1.00	5.00	19.91	0.070	0.016
12	0.17	0.67	0.17	66.92	92.41	0.118	1.574
13	1.00	0.00	0.00	20.42	60.15	2.547	0.129
14	0.50	0.50	0.00	56.15	97.71	0.488	3.658

proportions of each component (ZVI,  $\rm H_2O_2$  and pH) (Table 3). All experimental runs were performed in CBPR. In order to find an optimal composition for the performance of the heterogeneous Fenton-type process, the following responses were selected; mineralization and decolourization extents ( $X_{\rm TOC}$  and  $X_{\rm colour}$ ), and the final concentration of Fe(II) and Fe(III) in the system. Optimization criteria are given in Table 4.

The *Design-Expert 6.0.6* software package (Stat-Ease, Inc.) was used. All the mixture models used correspond to quadratic or special cubic Scheffé models, Eqs. (14) and (15) [24]. Note that E(X) stands for the corresponding model response.

$$E(X) = \sum_{i} \beta_{i} x_{i} + \sum_{i < j} \beta_{ij} x_{i} x_{j}$$

$$\tag{14}$$

$$E(X) = \sum_{i} \beta_{i} x_{i} + \sum_{i < j} \beta_{ij} x_{i} x_{j} + \sum_{i < j < k} \sum_{i < j < k} x_{i} x_{j} x_{k}$$

$$\tag{15}$$

The  $\Sigma \beta i \, x_x$  term is called the linear blending term, and the quadratic and cubic terms are called non-linear blending terms. If  $\beta ij$  is positive, the term is synergistic, while if it is negative it is called antagonistic.

Optimization was performed using the desirability function approach [2].

# 2.4. Experimental procedure

The model solution was prepared by dissolving RB1 in distilled water ( $\gamma(RB1)_0$  = 140 mg L<sup>-1</sup>; initial TOC value:  $\gamma(OC)_0$  = 31 mg L<sup>-1</sup>). The initial pH of the model solution was adjusted using the pH meter (Handylab pH/LF 12, Schott, Germany) for the pH control. In all the experiments, a desired amount of ZVI powder was uniformly spread on the reaction wall/bottom prior to the filling of reaction space with the model solution.

Photo-Fenton catalytic cycle in CBPR (UV-C/ZVI-Fenton) started with the simultaneous addition of hydrogen peroxide and irradiation start-up. In the BFSR (solar ZVI-Fenton), the flow rate of the model solution and the liquid level were set before the addition

**Table 4**Optimization criteria and results.

Goal	Criteria	Result	Desirability	
		Coded composition	Actual conditions	
		01	01	01
	$\gamma(Fe^{2+}), \gamma(Fe^{3+}) \Rightarrow minimum$	A = 0.25	m(ZVI) = 0.225 g	92.0%
	/(10 ), /(10 ) /	B = 0.44	$[H_2O_2] = 0.044 \text{ mol } L^{-1}$	
		C = 0.31	pH = 3.55	
$X_{TOC}, X_{colour} \Rightarrow \text{maximum}$	O1: A, B, C in range		•	
to t		02	02	02
	O2: $A \Rightarrow 0.2$	A = 0.21	m(ZVI) = 0.205 g	94.4%
	B in range	B = 0.38	$[H_2O_2] = 0.044 \text{ mol } L^{-1}$	
	$C \Rightarrow 0.45$	C = 0.42	pH = 4.10	

of  $H_2O_2$ . Experiments were carried out for 30 min (otherwise indicated).

#### 2.4.1. Additional and control experiments

In order to estimate the production of Fe(II) upon corrosion of ZVI in the acidic media, set of experiments were performed in the RB1 model solution, varying the amount of ZVI spread on the wall of CBPR and pH value of the media. Samples were taken every 30 s during the 5 min of the corrosion process. Corrosion experiments were performed under ambient light without the addition of  $\text{H}_2\text{O}_2$ . ZVI corrosion was also tested in distilled water at established optimal ZVI dosage and pH (pH 3.55).

Several control experiments were performed; photo-Fenton process with no addition of  $\rm H_2O_2$  (UV-C/ZVI), Fenton process performed under ambient light (ZVI-Fenton) and experiment with only  $\rm H_2O_2$  and irradiation (UV-C/ $\rm H_2O_2$ ). All of these processes were performed in CBPR.

Possibility of adsorption and reduction of RB1 on ZVI surface was also explored. Set of control experiments included stirring of the dye model solution in CBPR in dark (without UV-C lamp) at different pH conditions and with different ZVI loadings on reactor wall.

In order to determine RB1 photolysis rates, RB1 model solution was being illuminated with UV-C and solar irradiation for 60 min (Table 1).

#### 2.5. Measurements, analyses and calculations

Irradiation intensity was measured by radiometer UV-X, UVP, with the corresponding sensors for UV-C, UV-B and UV-A irradiation (UVX-25, UVX-31 and UVX-36). Intensity of the UV-C irradiation at 1 cm distance from the lamp wall was 126 mW cm $^{-2}$ . This is considered as the average intensity in the annular reaction space in CBPR. Additionally, intensity of incident irradiation ( $I_0$ ) was determined on the basis of chemical actinometry measurements according to the semiempirical model based on Lambert–Beer's law (LLM) [16].

$$-\frac{\mathrm{d}C_i}{\mathrm{d}t} = F_i \Phi_i I_0 \left( 1 - e^{-2.303 \cdot \mathrm{L} \cdot \sum \varepsilon_i C_i} \right) \tag{16}$$

where  $F_i$  represent the fraction of absorbed radiation by specie i (Eq. (17)),  $I_0$  and L represent the intensity of incident irradiation and effective path of radiation through the photoreactor, respectively, and  $\Phi_i$  and  $\varepsilon_i$  are quantum yield and molar absorption coefficient of a specie i at the wavelength of the irradiation source, respectively,

$$F_i = \frac{\varepsilon_i C_i}{\sum_{i=1}^n \varepsilon_i C_i} \tag{17}$$

Actinometry was performed using the potassium iodide/iodate (KI/KIO<sub>3</sub>) actinometer solution (0.6 mol L<sup>-1</sup> KI and 0.1 mol L<sup>-1</sup> KIO<sub>3</sub> in a 0.01 mol L<sup>-1</sup> Na<sub>2</sub>B<sub>4</sub>O<sub>7</sub> buffer solution;  $\Phi$  = 0.6,  $\varepsilon$  = 26,303 mol<sup>-1</sup> L cm<sup>-1</sup>)

[25]. Calculated  $I_0$  was  $1.05 \times 10^{-4}$  Einstein dm $^{-3}$  s $^{-1}$ , while irradiation path length in CBPR (L) was 1.45 cm.

The intensity of UV-A and UV-B irradiation (380 nm >  $\lambda$  > 290 nm) of direct sunlight was estimated at 6.9  $\pm$  2.8 mW cm<sup>-2</sup>. This is the integrated value obtained according to the measurements performed each 2 h between 11 am and 3 pm on sunny days in May and June (45° north latitude). Note that the standard global UV irradiance is 3 mW cm<sup>-2</sup> [26].

Mineralization extents  $(X_{TOC})$  and OC oxidation kinetics were determined on the basis of total organic carbon content measurements (TOC), performed by using a total organic carbon analyzer; TOC-V<sub>CPN</sub> 5000 A, Shimadzu. Decolourization extents ( $X_{colour}$ ) and RB1 oxidation kinetics was monitored spectrophotometrically using the UV-vis spectrophotometer, Lambda EZ 201, Perkin Elmer, at  $\lambda_{\text{max,RB1}}$  = 590 nm. Since the RB1 molar extinction coefficient,  $\varepsilon_{590\text{nm}}$ , varies up to 3% according to the initial pH (pH 2–7), absorbance of initial dye solution was checked prior to all experiments. However, position of the maximum absorbance (590 nm) does not change with pH. The concentration of ferrous ions and hydrogen peroxide in the bulk was determined by colorimetric methods as given in our previous publication [27]. The dissolvedoxygen concentration in the reaction media was continuously monitored with an Ingold model 34 100 3002 Clark-type probe (Mettler Toledo).

**Table 5**Mixture models.

Model response	Model equation
X <sub>TOC</sub> (%)	17.80 A + 52.08 B + 0.34 C + 110.91 AB - 18.79 AC - 28.71 BC + 950.45 ABC
$X_{ m colour}$ (%)	55.18 A + 95.00 B + 31.33 C + 100.59 AB + 11.05 AC + 164.77 BC
[Fe <sup>2+</sup> ] (mmol L <sup>-1</sup> )	2.46 A + 0.34 B + 0.09 C - 4.50 AB - 4.74 AC + 0.03 BC
[Fe <sup>3+</sup> ] (mmol L <sup>-1</sup> )	0.26 A + 2.61 B + 0.16 C + 7.98 AB - 1.28 AC - 6.98 BC

**Table 6**Statistics summary.

Model response	<i>X</i> <sub>TOC</sub> (%)	$X_{ m colour}$ (%)	$\gamma(\text{Fe}^{2+})$ (mg L <sup>-1</sup> )	$\gamma(\text{Fe}^{3+})$ $(\text{mg L}^{-1})$
Scheffé model	Special cubic	Quadratic	Quadratic	Quadratic
LOF* p-value	0.0844	0.0763	0.0743	0.3601
Model p-value	0.0005	0.0007	< 0.0001	0.0002
Model F-value	19.86	13.96	42.76	20.44
$R^2$	0.9445	0.8612	0.9500	0.9274
Adjusted R <sup>2</sup>	0.8970	0.7995	0.9278	0.8821

<sup>\*</sup> LOF - lack of fit.

The BET surface areas, pore volumes and pore size distribution were estimated from nitrogen adsorption and desorption isotherm data using an ASAP 2000 apparatus (Micromeritics Corporation). Prior to analysis, samples were degassed (6.6 Pa) at  $400\,^{\circ}\text{C}$  to remove any physically adsorbed gases. The pore size distributions of the samples were determined by the BJH (Barret–Joyner–Halenda) model from the data of adsorption and desorption branch of the nitrogen isotherms.

Morphology of the ZVI surface and the chemical composition (Fe, O) before and after the reaction was analyzed by scanning electron microscopy (SEM), MiraScan FEG SEM (TeScan) with an energy-dispersive X-ray analyzer (EDX) unit (Bruker).

100

Differential equations were solved using the finite difference method in Mathematica 7.0. Multiple linear regression analysis was performed using the Polymath v6.10.

# 3. Results and discussion

# 3.1. Experimental design and optimization

Mixture design analysis resulted in the mixture models that describe the mineralization and decolourization extents ( $X_{\rm TOC}$  and  $X_{\rm colour}$ ) and the residual concentration of Fe(II) and Fe(III) in the reaction media as a function of initial mixture composition (Table

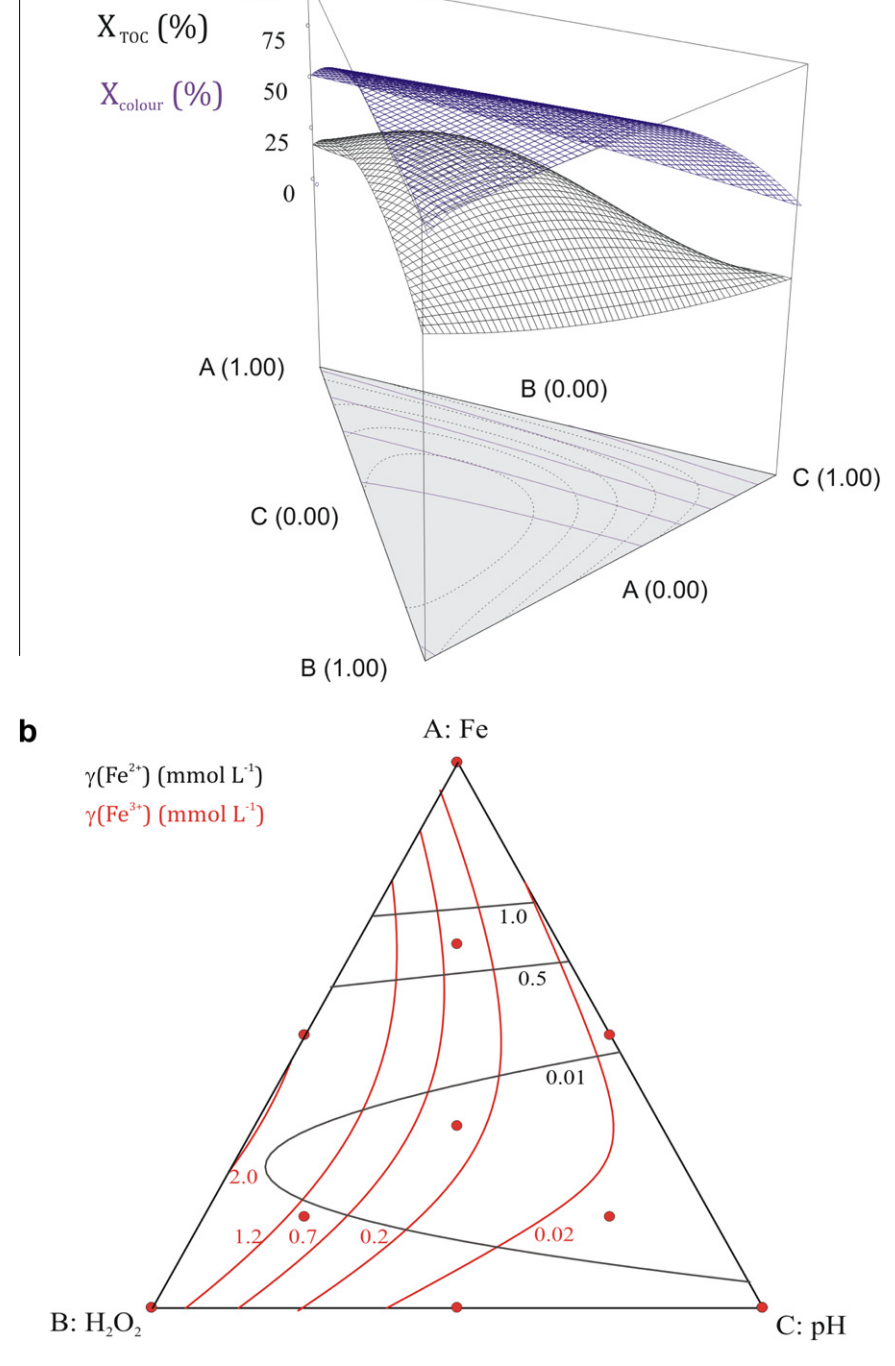


Fig. 3. Results of a mixture design analysis; graphical interpretation of the models, (a) for mineralization and decolourization extents, and (b) final concentration of Fe(II) and Fe(III) ions as a function of the mixture (Fe $^0$ , H<sub>2</sub>O<sub>2</sub> and pH) composition.

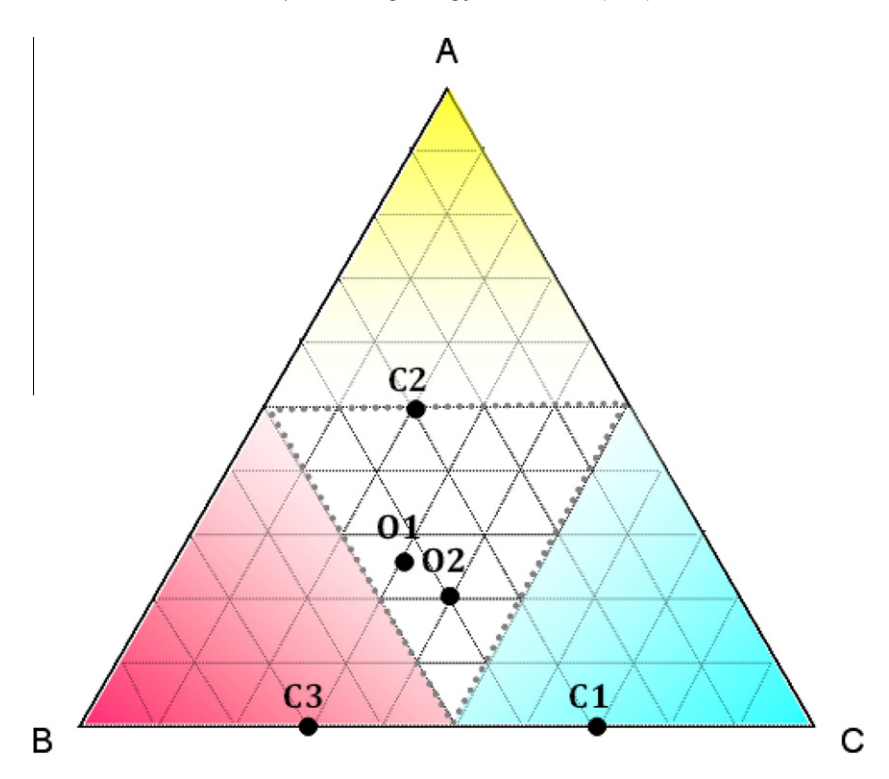


Fig. 4. Ternary diagram; dominant effect of single mixture component (colored areas at vertices), result of multi-criteria optimization (optimal points – O1, O2) and control points (C1, C2, C3).

5, Fig. 3). Mixture models were evaluated using ANOVA. Statistics summary was given in Table 6. F-values from 13.96 to 42.76 and p-values less than 0.05 imply that the models are significant. Lack of fit is not significant (p > 0.05). The fit of the experimental results is good ( $R^2$  values from 0.8612 to 0.9445). The obtained models showed a satisfying accuracy and adequacy over the selected design space.

Key parameters of Fenton process (Fe<sup>0</sup>, H<sub>2</sub>O<sub>2</sub> and pH) were treated as components of mixture due to the assumption that studying their proportions other than total amounts would lead to better optimization results. According to the ternary diagram (Fig. 4) that shows the proportions of the studied mixture components, the increase in the amount of one component (e.g. A) leads to a decrease of at least one of two other components. In the "mid" composition of the mixture (dashed triangle, Fig. 4), the portion of each component is less than 0.5, which corresponds to the expected optimal working area for the Fenton process. However, if one particular component highly affects the process performance, the optimal area would move towards the corresponding vertex (colored areas, Fig. 4). E.g., if component A drastically enhances process performance, optimal point would lay in yellow field (Fig. 4). Using the multi-criteria optimization approach, it is quite simple to obtain one single optimal point in design space. By varying the set criteria and their importance, it can be navigated throughout the design space. Set optimization criteria (Table 4) included maximization of  $X_{TOC}$  and  $X_{colour}$  with a simultaneous minimization of Fe(II) and Fe(III) generation. It might seem contradictory knowing the nature of Fenton process, but this optimization goal/criteria selection results in the single optimal point due to the constraints of the mixture design. Optimal composition (O1) simultaneously includes smaller amounts of ZVI and H<sub>2</sub>O<sub>2</sub> and a slightly acidic pH conditions. Additional optimization criteria lead to another optimal point (O2) whereas pH value of the system is even more increased (Table 4, Fig. 4). Furthermore, the three control points (C1, C2, C3) were obtained (Fig. 4) to test the validity of the performed analysis and the mixture models. As shown in Table 7, predicted  $X_{\rm TOC}$  and  $X_{\rm colour}$  correspond to the experimentally obtained values.

#### 3.2. ZVI corrosion

ZVI surface goes under corrosion prior initializing the Fenton reaction and during the photo-Fenton process. The initial period when Fe(II) ions are generated by corrosion on the ZVI surface is referred as *set time* ( $t_s$ ). Experimental data showed the increase of ferrous ions in the bulk solution during  $t_s \le 15$  min, following the apparent linear trend in  $t_s < 5$  min (Fig. 5).

After the selected  $t_S$  (1 or 5 min in both reactors, CBPR and BFSR), initial Fe<sup>2+</sup> concentration reaches the desired value. Regardless to selected  $t_S$ , concentration of Fe<sup>2+</sup> ions in  $t_S$  is considered as the initial Fe(II) ions concentration for the photo-Fenton process,

**Table 7**Predicted vs. experimental values of the mineralization and decolourization extents for optimal points and control points in the mixture.

	Selected checkpoints					
	01	02	C1	C2	С3	
Mixture composition						
Α	0.25	0.21	0	0.50	0	
В	0.44	0.38	0.30	0.30	0.70	
С	0.31	0.42	0.70	0.20	0.30	
X <sub>TOC</sub> (%) Experimental Model R <sup>2</sup>	54.3 62.6 0.9636	51.1 56.9	14.7 9.7	58.6 66.0	21.9 30.7	
X <sub>colour</sub> (%) Experimental Model	99.5 99.4	99.4 94.8	93.0 84.7	94.3 88.2	99.5 100	
R <sup>2</sup>	0.9170					

 $[Fe^{2+}]_0$ . The rate of Fe(II) production in  $t_S$  is given through the empirical model (see Section 2.4.1).

$$r_{t_s}(\text{Fe}^{2+}) = a_0(\Gamma_{\text{A.Fe}^0})^{a_1} \text{pH}^{a_2}$$
 (18)

where  $\Gamma_{A,Fe^0}$  represent the mass concentration of ZVI per surface and working volume, A and  $V_R$ , respectively.

$$\Gamma_{\rm A,Fe^0} = \frac{m_{\rm Fe^0}}{{\rm A}\times{\rm V_R}} \tag{19}$$

Estimated coefficients of the empirical model for the Fe(II) production during set time ( $t_S < 5 \text{ min}$ ) are;  $a_0 = 0.105 \text{ mol L}^{-1} \text{ min}^{-1}$ ,  $a_1 = 0.207$ ,  $a_2 = -3.688$ .

Since oxygen plays crucial role in the generation of Fe(II) ions by enhancing the corrosion rate [16], concentration of dissolved oxygen was monitored in  $t_S$  and during photo-Fenton process in CBPR (Fig. 6). In the beginning of  $t_S$ , model solution is about 77% saturated with  $O_2$ , which corresponds to 6.9 mg  $L^{-1}$ . Dissolved oxygen concentration is reduced during the first 10 min in  $t_S$  to the concentration of 2.3 mg  $L^{-1}$ . This can be ascribed to the corrosion of ZVI by

reaction with dissolved oxygen, Eq. (4)–(6) [15,16]. Upon the addition of  $H_2O_2$  and irradiation,  $O_2$  concentration slightly increases to the 3.4 mg  $L^{-1}$ . Finally, the constant value is obtained  $(2.5 \text{ mg } L^{-1})$ . Since there was no additional introduction of  $O_2$  in the reaction media, the effect of dissolved oxygen is not considered important for the kinetics of the studied Fenton process.

Due to the ZVI surface corrosion, there is a significant difference in the morphology and chemical composition of the surface (Fig. 7). ZVI surface has uniform morphology where Fe atoms are concentrated in spheres (aggregates), while the surface of the corroded material has a more cotton-like structures over spheres. EDX analysis showed the existence of O atoms on the surface of corroded ZVI, which corresponds to the theoretical corrosion products, i.e. iron oxides present on corroded ZVI surface [28]. The percentage of O atoms on corroded ZVI surface was estimated at 40.9-45.5%. It needs to be pointed out that corroded ZVI surface refers to the ZVI powder collected from the reactor wall after  $t_{\rm S}$  = 15 min.

Characterization of ZVI powder and corroded ZVI was also brought by gas adsorption–desorption porosimetry method. Different parameters, pore size distribution (PSD), average pore diameter

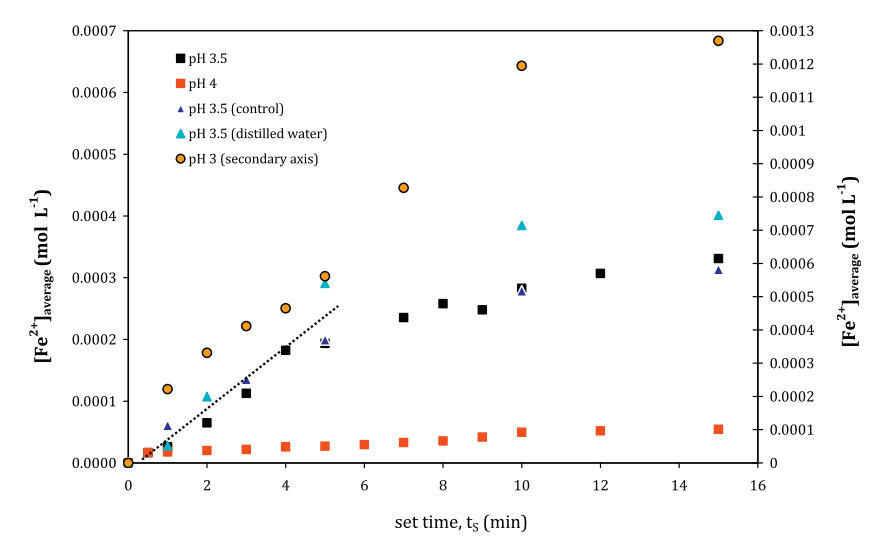
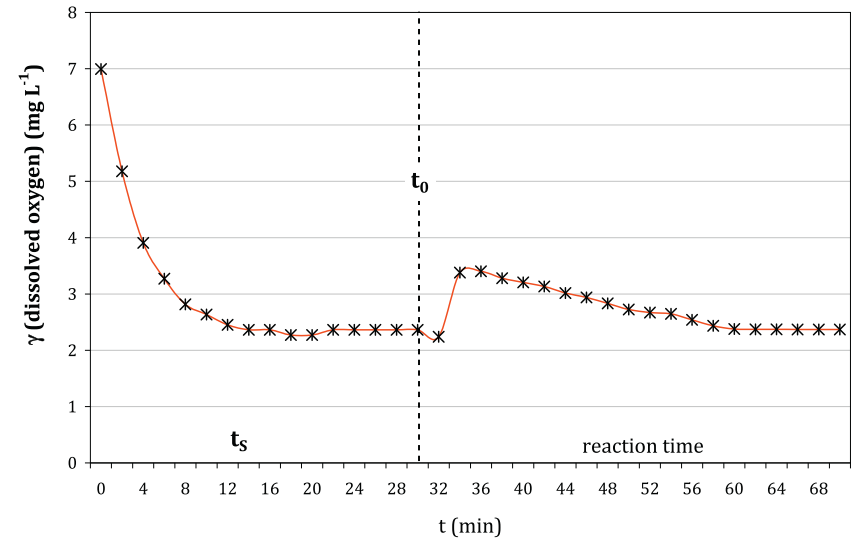


Fig. 5. Examples of Fe(II) leaching in bulk RB1 model solution and distilled water during set time ( $t_S < 15 \text{ min}$ ), m(ZVI) = 0.225 g at different pH values.



**Fig. 6.** Dissolved oxygen concentration during set time,  $t_S = 30$  min, and UV-C/ZVI-Fenton process (O1).

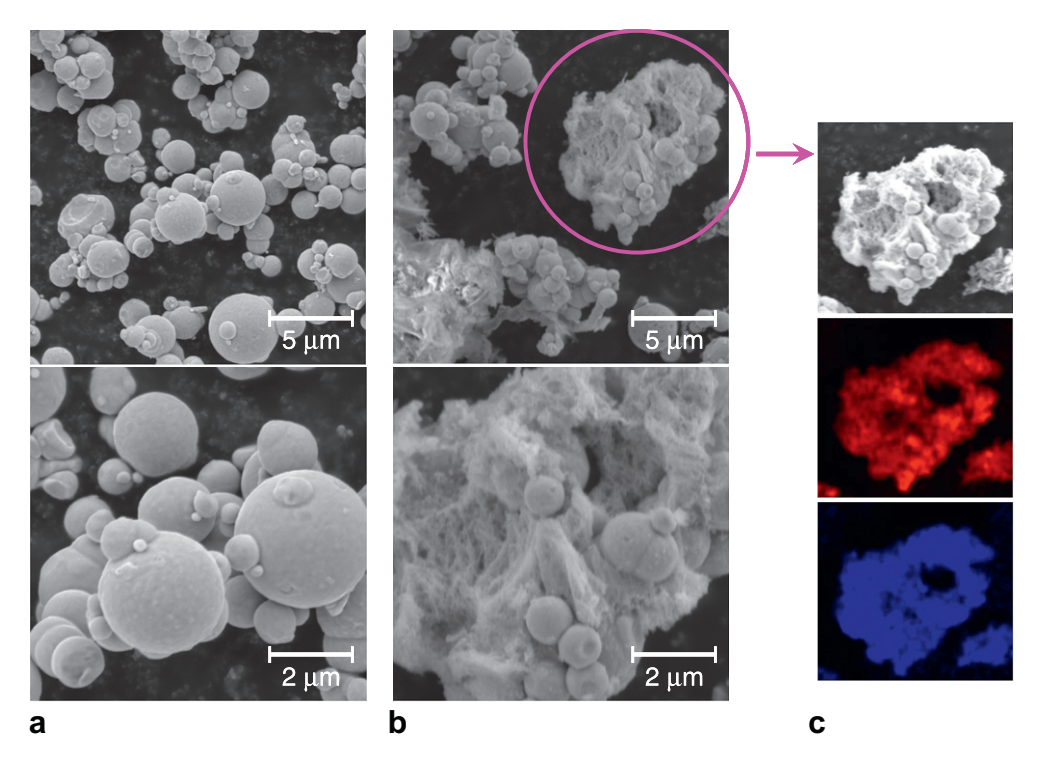


Fig. 7. SEM photomicrographs: (a) surface of ZVI powder and (b) corroded ZVI; (c) EDX analysis – Fe (red) and O (blue areas). (For interpretation of the references to colour in this figure legend, the reader is referred to the web version of this article.)

and BET surface area were studied and related to the scanned morphology. Pore size distribution of initial ZVI sample shows monodisperse pore structure with distinct narrowness of frequency distribution of pore sizes around 3–5 nm (Fig. 8). Contrary, structure of corroded ZVI catalyst is characterized with wide distribution of pore sizes (2–170 nm) positioned at high pore radii values (Fig. 8). Such significant difference in PSDs was also noted within attendance of higher values of average pore diameter (6.7772 vs. 14.8050 nm) and BET surface area (0.5855 vs. 2.9542 m² g<sup>-1</sup>).

Remarked PSDs variety validates some transformations in morphology of ZVI catalyst upon corrosion. Deposits of iron oxides on ZVI surfaces, confirmed with EDX analysis, render as fibrous structure scattered over spheres. Such cotton-like structure is a very porous and usually contributes to high-voluminous character of

material [29,30]. Consequently, attained morphology (Fig. 7) brings such a scattered distribution of pore sizes within corroded ZVI catalyst (Fig. 8).

#### 3.3. Kinetic study

# 3.3.1. Heterogeneous vs. homogeneous catalysis approach

Two approaches have been applied to study the kinetics of UV-C/ZVI-Fenton process in CBPR. Heterogeneous catalytic pathway has been assumed in the first approach, while the second approach dealt with the pure homogeneous catalysis, concentrating on the role of Fe(II) ions in the bulk solution due to its leaching from corroded ZVI surface. Heterogeneous kinetic model serves as usual approximation for degradation kinetics by ZVI related processes

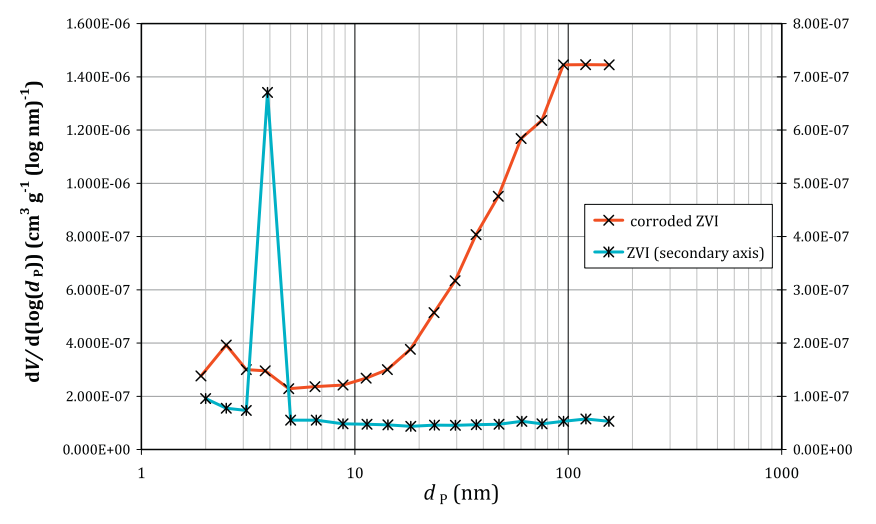
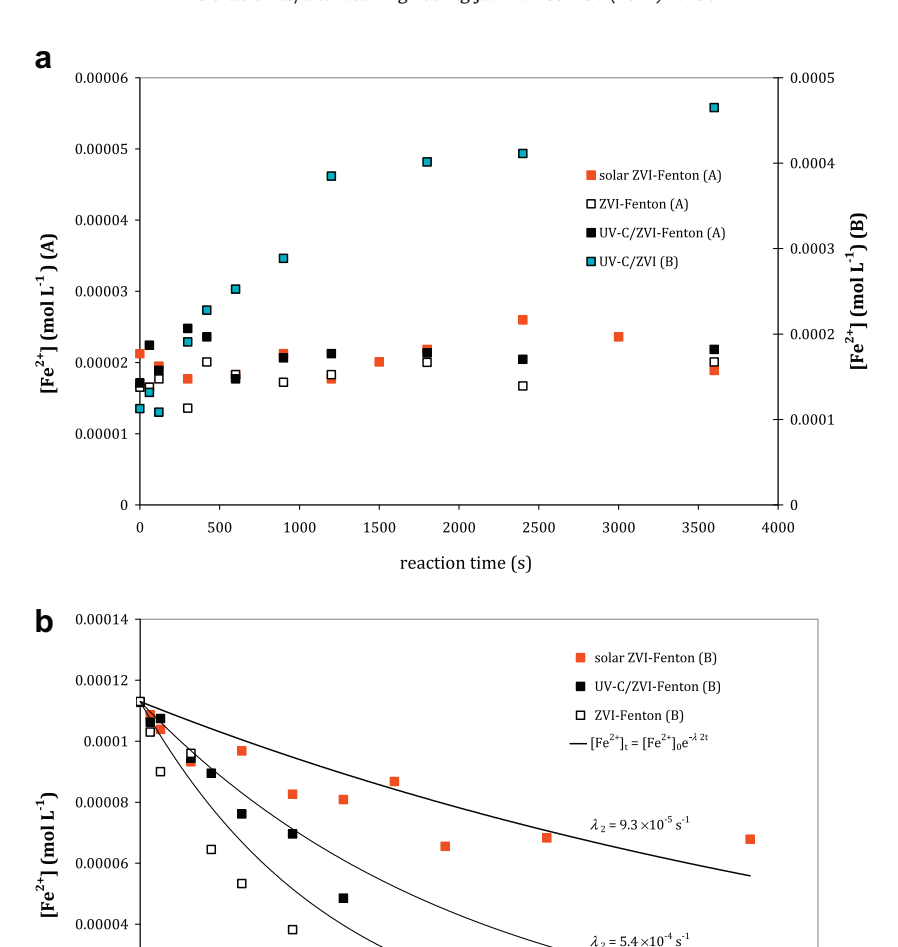


Fig. 8. Pore size distribution from BJH model: ZVI powder vs. corroded ZVI.



**Fig. 9.** Concentration profile of Fe(II) ions in different combination of ZVI-Fenton processes at optimal process conditions (O1), (a) apparent constant concentration after  $t_S = 1$  min and further Fe(II) leaching in UV-C/ZVI process ( $t_S = 5$  min); (b) exponential decrease of Fe<sup>2+</sup> concentration after  $t_S = 5$  min.

2000

reaction time (s)

2500

3000

3500

п

1500

1000

[16]. In the same manner, OC oxidation kinetics during UV-C/ZVI-Fenton process can be described by pseudo-first-order kinetics with the observed rate constant  $k_{\rm obs}$ .

0.00002

0

0

500

$$OC \frac{Fe^0, H_2O_2}{h\nu}$$
 inorganic products (20)

$$r_{\rm OC} = -d[{\rm OC}]/dt = k_{\rm obs}[{\rm OC}] \tag{21}$$

However, the observed rate constant varies according to the set experimental conditions and it is constant for a limited range of experimental conditions. During ZVI-Fenton processes, ZVI amount and the corresponding surface area have the crucial effect on the  $k_{\text{obs}}$ , and therefore, it is important to define specific reaction rate constant,  $k_{\text{SA}}$  [16].

$$k_{\text{obs}} = k_{\text{SA}} \times \rho_{\text{a}} = k_{\text{SA}} \times a_{\text{S}} \times \rho_{\text{M}} \tag{22}$$

where  $\rho_a$  is the concentration of iron surface area (m<sup>2</sup> L<sup>-1</sup>),  $a_S$  is the specific surface area measured by BET gas adsorption (0.5855 m<sup>2</sup> g<sup>-1</sup>), and the  $\rho_M$  is the catalysts mass concentration (ZVI mass divided by working volume, g L<sup>-1</sup>).

The results of the heterogeneous kinetic model applied in this study are given in Table 8. As it can be seen,  $k_{SA}$  increases in the acidic media (lower pH). In UV-C/ZVI process (with no addition

of H<sub>2</sub>O<sub>2</sub>), an *in-situ* generation of was observed (Fig. 10). Nevertheless, the corresponding values of  $k_{SA}$  are significantly lower (Table 8). In addition, control experiments of RB1 adsorption and reduction on ZVI surface resulted with maximum of 4% of decolourization yield, while no reduction in TOC values was observed. The observed results indicate the more complex reaction pathway. Therefore, homogeneous catalysis might be the better approximation of an ongoing process. In acidic media, ZVI goes under corrosion, releasing the Fe(II) ions in the bulk solution. As stated previously, Fe(II) concentration increase during set time, giving the adequate amount of Fe(II) ions for Fenton reaction cycle. Under the assumption of well-mixing, Fe(II) ions react instantaneously with H<sub>2</sub>O<sub>2</sub> in the bulk solution and the hydroxyl radicals, OH, are generated in each point of the reaction space. Following the homogeneous catalysis, ZVI is considered only as a source of Fe(II) ions for the Fenton reaction cycle.

4000

#### 3.3.2. Homogeneous model for the Fenton-type processes

Developed model for the homogeneous catalysis reflects on two issues; (i) rate of Fe(II) production from ZVI surface, and (ii) rate of reaction between organic content (OC) or dye (RB1) with 'OH radicals in the frame of formal kinetic scheme for the Fenton process [23,31].

**Table 8** Specific reaction rate constant in the heterogeneous kinetic model in CBPR; m(ZVI) = 0.225 g,  $[H_2O_2] = 0.044 \text{ mol L}^{-1}$ .

	pH = 3.5				pH = 5
	ZVI-Fenton	UV-C/ZVI-Fenton	UV-C/ZVI	UV-C/ZVI-Fenton	UV-C/ZVI-Fenton
$k_{SA} (L \min^{-1} m^{-2})$	$6.028  imes 10^{-3}$	0.0205	$1.256 \times 10^{-3}$	0.0192	0.0122

After ZVI corrosion in  $t_S$ , a certain amount of Fe(II) is generated (see Section 3.2). The concentration of Fe(II) in  $t = t_S$  represent the initial concentration of Fe(II) ions for Fenton reaction, while  $t_S$  is considered as the  $t_0$  of reaction.

$$t = t_S = t_0 \Rightarrow [Fe^{2+}]_{t_S} = [Fe^{2+}]_{t_0}$$
 (23)

Fenton reaction cycle starts upon the addition of  $H_2O_2$  and/or irradiation and Fe(II) ions are consumed. Due to the simultaneous generation and consumption of ferrous ions in the reaction media, Fe(II) concentration can be considered constant, Eq. (24) (Fig. 9a). In the case of longer  $t_S$ , Fe(II) ions are consumed following the exponential law with the observed rate constant,  $\lambda_2$  ( $s^{-1}$ ) (Fig. 9b).

$$[Fe^{2+}]_t = [Fe^{2+}]_{t_0} = const. \quad (\lambda_2 \approx 0 \text{ min}^{-1})$$
 (24)

$$[Fe^{2+}]_t = [Fe^{2+}]_{t_0} \times e^{-\lambda_2 t}$$
 (25)

To establish a kinetic model to describe Fenton reaction cycle, it was assumed that OC (or RB1) is primarily degraded by hydroxyl radicals. Accordingly, OC oxidation kinetics in CBPR and BFSR, given as a disappearance rate of OC, can be expressed as;

$$r_{\rm OC} = -d[{\rm OC}]/dt = k_1[{\rm OC}][{\rm OH}]$$
 (26)

where  $k_1$  (L mol<sup>-1</sup> s<sup>-1</sup>) represent the rate constant for the reaction between OC and 'OH radicals. The same equation was written for RB1 oxidation kinetics.

Following the crucial reactions of the Fenton catalytic cycle summarized by Wu et al. [23], and having in mind the most important ones; Eqs. (27)–(29) [23,31];

$$Fe^{2+} + H_2O_2 \xrightarrow{k_2(r_2)} Fe^{3+} + OH + OH^-$$
 (27)

$$H_2O_2 + OH \xrightarrow{k_3(r_3)} H_2O + HO_2$$
 (28)

$$Fe^{2+} + OH \xrightarrow{k_4(r_4)} Fe^{3+} + OH^-$$
 (29)

Final equation for the OC oxidation rate in CBPR and BFSR (**homogeneous kinetic model**) has the following form [31].

$$r_{OC} = -\frac{d[OC]}{dt} = k_1[OC][OH]$$

$$= k_1 \frac{k_2[Fe^{2+}]_0[H_2O_2]_0 e^{-\lambda_1 t} e^{-\lambda_2 t}}{k_1[OC] + k_3[H_2O_2]_0 + k_4[Fe^{2+}]_0}[OC]$$
(30)

where  $\lambda_1$  (s<sup>-1</sup>) represent the rate of the  $H_2O_2$  consumption during the studied Fenton process (Fig. 10). Similar equation is obtained for RB1 oxidation rate. Concentration profiles of  $H_2O_2$  during the performed Fenton type processes are shown in Fig. 10.

In addition to the adopted reaction scheme and the kinetic model [23,31], the reaction between Fe(II) and  $H_2O_2$  (Eq. (27)) is considered as a main source of 'OH radicals. However, under UV-C irradiation, 'OH radicals are also generated due to the photolysis of  $H_2O_2$  [16].

$$H_2O_2 + h\nu \xrightarrow{r_5} 2:OH(254 \text{ nm})$$
 (31)

Rate of 'OH generation can be described using the expression for the rate of photolysis according to the LLM (Eq. (16)). Furthermore, certain number of 'OH radicals is lost due to recombination.

$$2:OH \xrightarrow{k_6(r_6)} H_2O_2 \tag{32}$$

To include the effect of  $r_5$  and  $r_6$  on OC and RB1 oxidation rate, complex model was developed. Accordingly, generation rate of 'OH radicals is given by Eq. (33).

$$\begin{split} r_{\cdot \text{OH}} &= d[\text{OH}]/dt = r_2 - r_3 - r_4 + r_5 - r_6 - r_{\text{OC}} \\ &= k_2[\text{Fe}^{2+}][\text{H}_2\text{O}_2] - k_3[\text{OH}][\text{H}_2\text{O}_2] - k_4[\text{Fe}^{2+}][\text{OH}] \\ &+ \text{F}_{\text{H}_2\text{O}_2} \Phi_{\text{H}_2\text{O}_2} I_0 (1 - e^{-2.303\text{LA}_{254\text{nm}}}) - k_6[\text{OH}][\text{OH}] \\ &- k_1[\text{OC}][\text{OH}] \end{split} \tag{33}$$

Following the pseudo-steady state assumption  $(d[\cdot OH]/dt = 0)$  [23,31], the quadratic equation for concentration of  $\cdot OH$  radicals,  $[\cdot OH]_t$ , is obtained. After introducing the solution for  $[\cdot OH]_t$  in OC

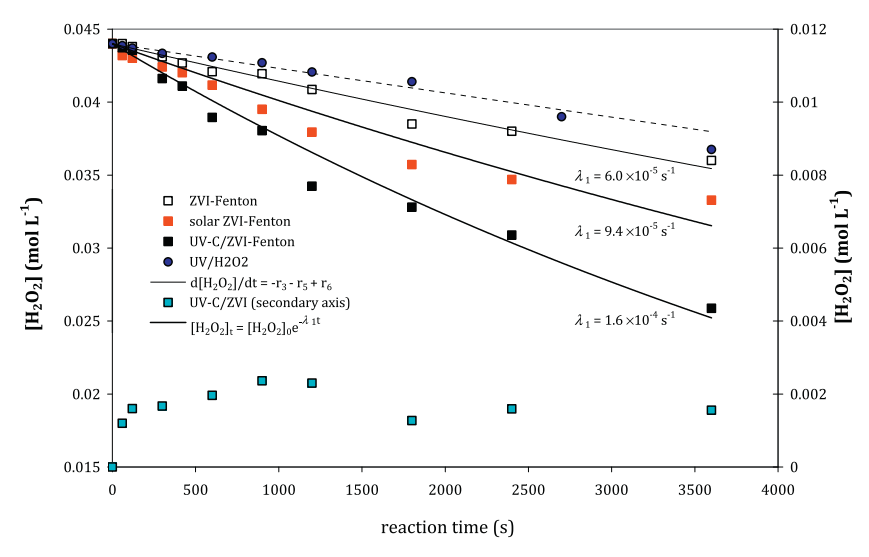


Fig. 10. Concentration profile of H<sub>2</sub>O<sub>2</sub>, in different ZVI-Fenton processes at optimal process conditions (O1), t<sub>SCBPR</sub> = 1–5 min and t<sub>SBFSR</sub> = 1–2 min.

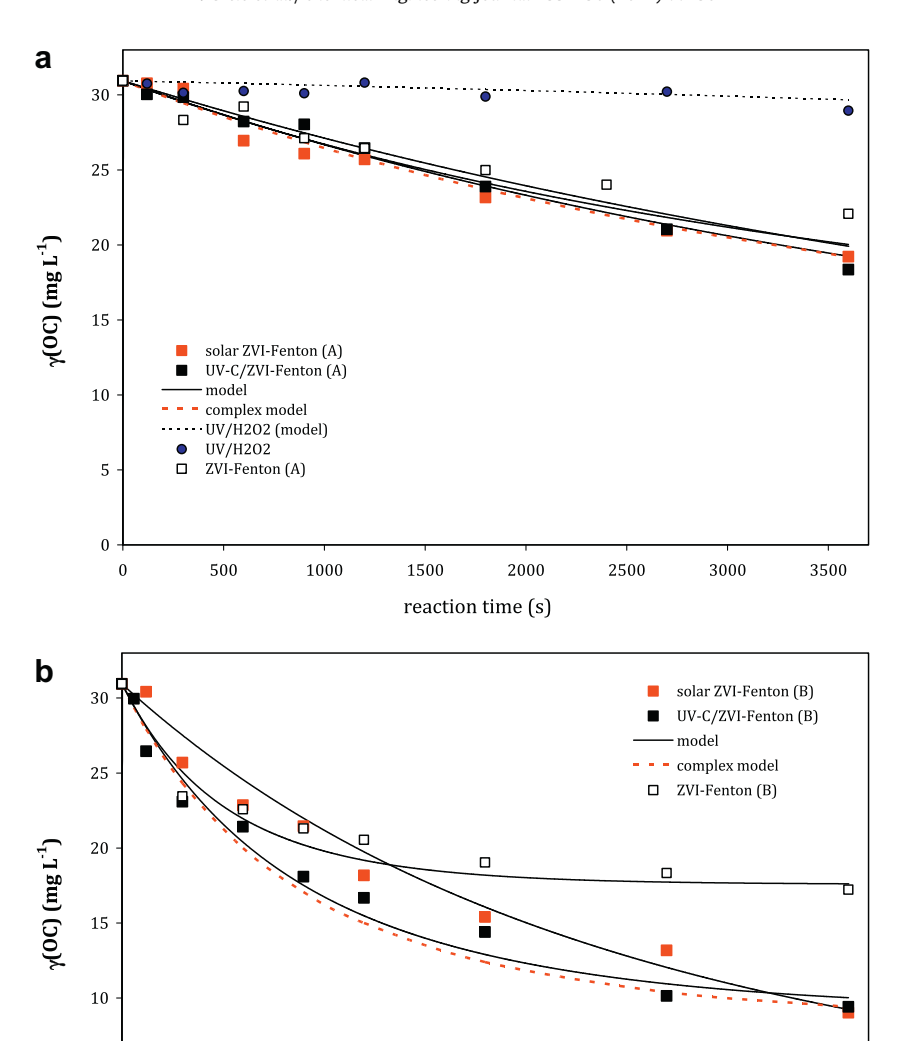


Fig. 11. Comparison of OC oxidation kinetics in model solution by different processes (O1 process conditions), (a)  $t_S = 1 \min(A)$  and (b)  $t_S = 5 \min(B)$ ; experimental vs. model values (homogeneous kinetic model – solid line, complex model – dashed line).

reaction time (s)

2000

2500

3000

1500

and RB1 oxidation kinetic model (Eq. (26)), final equation of **complex model** is developed.

5

0 +

500

1000

$$\begin{split} r_{\text{OC}} &= -\frac{d|\text{OC}|}{dt} = \\ k_1 \left( \frac{-(k_1|\text{OC}|+k_3|\text{H}_2\text{O}_2|_0 + k_4|\text{Fe}^{2+}|_0)}{2k_6} + \\ \sqrt{(k_1|\text{OC}|+k_3|\text{H}_2\text{O}_2|_0 + k_4|\text{Fe}^{2+}|_0)^2 + 4k_6(k_2|\text{Fe}^{2+}|_0|\text{H}_2\text{O}_2|_0 e^{-\lambda_1 t} e^{-\lambda_2 t} + \text{Fi}_{\text{H}_2\text{O}_2} \Phi_{\text{H}_2\text{O}_2} I_0(1 - e^{-2303L\text{A}_{254nm}}))} \right) |\text{OC}| \end{split}$$

In order to get the solution to complex model, fraction of absorbed irradiation by  $H_2O_2$  ( $F_{H_2O_2}$ ) has to be well estimated. Therefore, absorbance of light at 254 nm by model solution/reaction system in whole was monitored during the experiments ( $A_{254\mathrm{nm}}$ ). These established value for  $A_{254\mathrm{nm}}$  is  $1.91 \pm 0.04$ . Apparently, it remained constant during all experiments.  $F_{H_2O_2}$  at certain periods of time is given in following equation.

$$F_{H_2O_2} = \frac{\epsilon_{H_2O_2}[H_2O_2]_t}{\frac{A_{254nm}}{1 \text{ cm}}} = \frac{\epsilon_{H_2O_2}e^{-\lambda_1 t}}{\frac{A_{254nm}}{1 \text{ cm}}}$$
(35)

Note that  $A_{254nm}/1$  cm corresponds with  $(\Sigma \epsilon_i c_i)_{254nm}$ . Control experiments were performed (UV-C/H<sub>2</sub>O<sub>2</sub>), Figs. 10, 11a and 12, to

validate the established assumptions. Experimental data for  $H_2O_2$ , OC and RB1 concentration fit well the values modeled according to the following Eqs. (36) and (37). Note that Eq. (37) is shortened complex model, obtained by excluding reactions that involve ferrous ions ( $r_2$  and  $r_4$ ).

3500

$$r_{\rm H_2O_2} = d[{\rm H_2O_2}]/dt = -r_3 - r_5 + r_6 \tag{36}$$

$$\begin{split} r_{\text{OC}}(or\,r_{\text{RB1}}) &= -\frac{d|\text{OC}|}{dt} = \\ k_1 \left( -\frac{(k_1|\text{OC}| + k_3|\text{H}_2\text{O}_2|_0)}{2k_6} + \frac{\sqrt{(k_1|\text{OC}| + k_3|\text{H}_2\text{O}_2|_0)^2 + 4k_6(F_{\text{H}_2\text{O}_2}\Phi_{\text{H}_2\text{O}_2}I_0(1 - e^{-2.303LA_{254nm}))}}{2k_6} \right) [\text{OC}] \end{split}$$

Results for OC and RB1 kinetics obtained by the developed homogeneous kinetic model (Eq. (30)) and complex model (Eq. (34)) were compared to the experimental data (Table 10). The fit is good with reasonably low normalized root mean square deviations. Resulting plots showing the OC and RB1 kinetics in the model solution are shown in Figs. 11 and 12. As can be seen from Fig. 11a, mineralization of RB1 model solution by UV-C/H<sub>2</sub>O<sub>2</sub> process can be considered negligible, i.e. only 6.52% reduction in TOC value is observed. At the

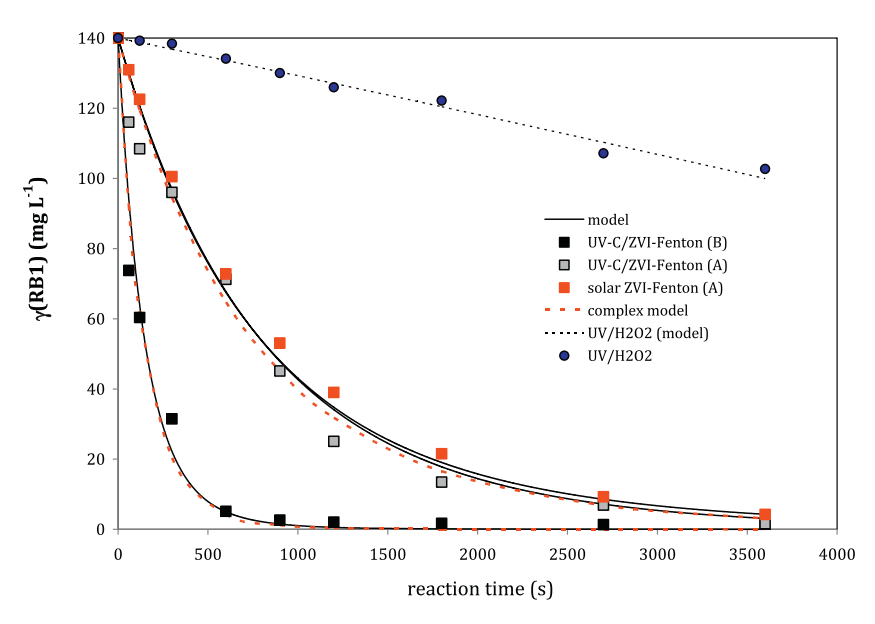


**Fig. 12.** RB1 oxidation kinetics in model solution by applied ZVI photo-Fenton processes at optimal process conditions, O1 ( $t_{S,CBPR} = 1 \text{ min (A)}$  and 5 min (B);  $t_{S,BFSR} = 1-2 \text{ min)}$ ; experimental vs. model values (homogeneous kinetic model – solid line, complex model – dashed line).

same time, somewhat higher extent of decolourization is achieved during 60 min of UV-C/H<sub>2</sub>O<sub>2</sub> process (26.67%) (Fig. 12).

The obtained results justify the applicability of both models, simple homogeneous kinetic model (Eq. (30)) and complex model (Eq. (34)), and the assumption that reaction between Fe<sup>2+</sup> and H<sub>2</sub>O<sub>2</sub> (Eq. (30)) is a main source of OH radicals for OC and RB1 oxidation in ZVI-Fenton processes. Due to simplification purposes, generation of OH radicals due to photolysis of H<sub>2</sub>O<sub>2</sub> and corresponding chain propagation and termination reactions [16] can be neglected. Furthermore, estimated values of  $k_1$  for OC and RB1 oxidation in CBPR are in accordance with the values estimated in BFSR.

Meanwhile, the possible influence of all ongoing reactions on concentration of reagents during the process was considered through the experimentally determined reagent consumption rates (constants  $\lambda_1$  and  $\lambda_2$ ), including the possible influence of  $O_2$ , irradiation or temperature oscillation. Constants  $\lambda_1$  and  $\lambda_2$  are not universal and they moderately vary depending on the experimental conditions. They are good approximation of the reagents' consumption and this approach significantly simplifies the modeling. However, the obvious lack is the necessary determination of  $\lambda_1$  and  $\lambda_2$  in new unexplored reaction systems. Parameters of the applied homogeneous model for the studied Fenton-type processes;  $k_1$  to  $k_6$ ,  $\lambda_1$ ,  $\lambda_2$  and initial concentration of reagents are summarized in Table 9.

#### 3.3.3. Effect of corrosion and applied irradiation

ZVI appeared as an adequate catalyst for Fenton processes, but only due to corrosion of its surface. To study the impact of ZVI corrosion on process performance, experiments were performed with two different set times, (A)  $t_S = 1$  min and (B)  $t_S = 5$  min. In the case A, initial concentration of Fe(II) ions in bulk model solution was about  $2 \times 10^{-5}$  mol L<sup>-1</sup>, resulting in the lower mineralization extents (Fig. 11a). It is evident that there is a certain balance between Fe(II) consumption and generation rates after  $t_S = 1 \text{ min (Fig. 9a)}$ . However, although [Fe2+] remained almost constant during 60 min of the process, the corresponding [Fe<sup>2+</sup>] is not enough to achieve satisfying mineralization extents. On the other hand, in case B, initial  $[Fe^{2+}]_0$  was about  $1.5 \times 10^{-4}$  mol  $L^{-1}$ , mineralization extents were higher (Fig. 11b), and [Fe<sup>2+</sup>] decrease exponentially with the apparent rate  $\lambda_2$  (Fig. 9b). The highest recorded concentration of Fe(II) and Fe(III) ions after 60 min of all applied ZVI Fenton processes were 4.7 and  $2.3 \times 10^{-4}$  mol L<sup>-1</sup>, respectively. The given values indicate the negligible secondary pollution by dissolved iron species.

According to the determined RB1 photolysis rates (Table 1) and the assumed low quantum yields of the expected aromatic byproducts [16], photolysis of both OC and RB1 was considered as negligible. On the other hand, type of the applied irradiation affects

**Table 9**Parameters of the homogeneous models for studied ZVI photo-Fenton processes (O1 process conditions).

Parameters	UV-C/ZVI-Fenton			Solar ZVI-Fenton			
	$t_S = 1 \text{ min}$		$t_S = 5 \min$		$t_S = 1 \min$		$t_S = 5 \text{ min}$
[Fe <sup>2+</sup> ] <sub>0</sub> (mol L <sup>-1</sup> )	$2.0\times10^{-5}$		$1.3 \times 10^{-4}$		$2.0 \times 10^{-5}$		$1.5 \times 10^{-4}$
$\lambda_1 (s^{-1})$		$1.6\times10^{-4}$				$9.4\times10^{-5}$	
$\lambda_2 (s^{-1})$	≈0		$5.4\times10^{-4}$		≈0		$9.3\times10^{-5}$
$k_1  (\text{L mol}^{-1}  \text{s}^{-1})$				$1.5 \times 10^{6} (OC)$			
				$1.2 \times 10^7  (RB1)$			
$k_2$ (L mol <sup>-1</sup> s <sup>-1</sup> )				170 [23,31]			
$k_3$ (L mol <sup>-1</sup> s <sup>-1</sup> )				$3.3 \times 10^7$ [23,31]			
$k_4$ (L mol <sup>-1</sup> s <sup>-1</sup> )				$3.2 \times 10^8$ [23,31]			
$k_6 (L \text{ mol}^{-1} \text{ s}^{-1})$				$5.5 \times 10^9$ [16]			
$\varepsilon_{\rm H202}~({\rm L}~{\rm mol}^{-1}~{\rm cm}^{-1}$	)	18.7 [16]				$\approx$ 0	
$\Phi_{H2O2}$		0.5 [16]					

**Table 10**Normalized root mean square deviations [27] for the application developed models to ZVI photo-Fenton processes (Figs. 11 and 12).

Process	Modeled value						
	OC		RB1				
	Homogeneous kinetic model	Complex model	Homogeneous kinetic model	Complex model			
UV-C/ZVI-Fenton (A)	0.0773	0.0741	0.1332	0.1276			
UV-C/ZVI-Fenton (B)	0.0655	0.0783	0.0351	0.0303			
Solar ZVI-Fenton	0.0248	_	0.0960	-			

the performance of Fenton process. Rate of H<sub>2</sub>O<sub>2</sub> consumption was observed in the following manner; UV-C > solar > dark (ZVI-Fenton) (Fig. 10, Table 9). Under UV-C irradiation, H<sub>2</sub>O<sub>2</sub> photolysis is emphasized due to the high value of its quantum yield  $(\Phi_{H_2O_2})$  at 254 nm. The  $\Phi_{\rm H_2O_2}$  significantly decreases with the wavelengths ranging from 290 to 600 nm [16,32]. Furthermore, iron complexes (-hydroxy, -oxalate and similar) present in the reaction media [2,17] show the interesting absorption characteristics by exhibiting total absorbance of all incident photons below 400 nm at relatively low molar concentrations. The absorption extends well into the visible range of the electromagnetic spectrum and decreases to zero at about of 550 nm [33]. Due to the high quantum yields, irradiation with  $\lambda \leq 400$  nm is responsible for the photo-transformation of iron (ferric) complexes and the generation of Fe(II) as a free cation in the aqueous solution (Eqs. (7) and (9)) [26,34]. The resulting Fe(II) concentration profiles (Fig. 9b) depicted the described phenomena. Rate of Fe(II) ions consumption is the highest in dark, while the concentration of ferrous ions is almost constant under the solar irradiation. In the system where H<sub>2</sub>O<sub>2</sub> is generated in-situ (UV-ZVI), concentration of Fe(II) ions increases with time (Fig. 9a) as a result of the simultaneous corrosion process and Fenton reaction. As a result of photo-transformation of iron complexes, additional Fe(II) ions are available for "new cycle" of Fenton reaction. This also explains the fast H<sub>2</sub>O<sub>2</sub> consumption rate in BFSR, especially because the photolysis of H<sub>2</sub>O<sub>2</sub> under solar irradiation is minimal due to the negligible flux of irradiation below 290 nm reaching the Earth surface.

## 4. Conclusions

Photo-Fenton process using the zero-valent iron (Fe<sup>0</sup>, ZVI) as a catalyst has been applied to study the oxidation in the model wastewater containing reactive azo dye, C.I. Reactive Black 1 (RB1). Novel reactor configurations have been presented; a cylindrical laboratory batch photo-reactor (CBPR) with the immobilized iron using the flexible magnetic stripes thus maximizing the surface area exposed to the irradiation and a boat-shaped solar reactor (BFSR) operated in total recirculation mode with the immobilized iron at the bottom.

Mixture design methodology has been applied to optimize the Fenton reagent and operating pH conditions. This design entails the constraints that narrow the optimization possibilities thus resulting with the single optimal point. Calculated optimal composition (O1) includes smaller amounts of ZVI and  $H_2O_2$  and a slightly acidic pH conditions. Additional optimization criteria (pH > 4) lead to another optimal point (O2).

Corrosion of ZVI surface at pH  $\leq$  4 resulted with three complementary phenomena: (i) slight degradation of initial uniform morphology; (ii) generation of iron oxides on ZVI surface and (iii) Fe(II) leaching into bulk solution. Mutual supplementation of SEM–EDX and porosimetry methods in material characterization is newly presented within these considerations.

Mineralization and dye degradation kinetics have been studied. Two approaches have been compared; heterogeneous vs. homogeneous catalysis. Due to better approximation of the overall process, homogeneous kinetic approach was introduced to ZVI-photo-Fenton modeling. ZVI was considered only as a source of Fe(II) ions, necessary for Fenton catalytic cycle. Model for homogeneous catalysis by ZVI-photo-Fenton processes was developed, with the estimated rate constants for the reaction between organic content and RB1 with 'OH radicals,  $k_1$ , of  $1.5 \times 10^6$  L mol<sup>-1</sup> s<sup>-1</sup> and  $1.2 \times 10^7$  L mol<sup>-1</sup> s<sup>-1</sup>, respectively. Adequate set time ( $t_S = 5$  min) assured the higher [Fe<sup>2+</sup>]<sub>0</sub> in bulk solution, while application of solar irradiation lowered the Fe(II) consumption rate,  $\lambda_2$ . Consequently, higher mineralization extents are achieved. Performance of ZVI-photo-Fenton process in the BFSR (solar ZVI-Fenton) offered a perspective for low cost Fenton processing of textile effluents.

#### Acknowledgments

This work was financially supported by the Croatian Ministry of Science, Education and Sport, Project #125-1253092-1981. The authors would like to express their gratitude to professor Đurđica Parac-Osterman and Zorana Kovačević (Faculty of Textile Technology at University of Zagreb) for SEM-EDX analysis, to assistant professor Zvjezdana Findrik for providing the oxygen electrode, and to Željko Pavlin Žac for ASAP measurements.

#### References

- L. Gomathi Devi, S. Girish Kumar, K. Mohan Reddy, C. Munikrishnappa, Photodegradation of Methyl Orange an azo dye by Advanced Fenton Process using zero valent metallic iron: Influence of various reaction parameters and its degradation mechanism, J. Hazard. Mater. 164 (2009) 459–467.
- [2] I. Grčić, D. Vujević, J. Šepčić, N. Koprivanac, Minimization of organic content in simulated industrial wastewater by Fenton type processes: a case study, J. Hazard. Mater. 170 (2009) 954–961.
- [3] C.S.D. Rodrigues, L.M. Madeira, R.A.R. Boaventura, Treatment of textile effluent by chemical (Fenton's Reagent) and biological (sequencing batch reactor) oxidation, J. Hazard. Mater. 172 (2009) 1551–1559.
- [4] M. Pérez, F. Torrades, X. Domènech, J. Peral, Fenton and photo-Fenton oxidation of textile effluents, Water Res. 36 (2002) 2703–2710.
- [5] S.H. Lin, M.L. Chen, Purification of textile wastewater effluents by a combined Fenton process and ion exchange, Desalination 109 (1997) 121–130.
- [6] S. Meric, H. Selçuk, V. Belgiorno, Acute toxicity removal in textile finishing wastewater by Fenton's oxidation, ozone and coagulation-flocculation processes, Water Res. 39 (2005) 1147–1153.
- [7] J.C. Garcia, J.L. Oliveira, A.E.C. Silva, C.C. Oliveira, J. Nozaki, N.E. de Souza, Comparative study of the degradation of real textile effluents by photocatalytic reactions involving UV/TiO2/H2O2 and UV/Fe2+/H2O2 systems, J. Hazard. Mater. 147 (2007) 105–110.
- [8] S. Nachiappan, K. Muthukumar, Intensification of textile effluent chemical oxygen demand reduction by innovative hybrid methods, Chem. Eng. J. 163 (2010) 344–354.
- [9] Shyh-Fang Kang, Chih-Hsaing Liao, Mon-Chun Chen, Pre-oxidation and coagulation of textile wastewater by the Fenton process, Chemosphere 46 (2002) 923–928.
- [10] Shyh-Fang Kang, Chih-Hsiang Liao, Shei-Tue Po, Decolorization of textile wastewater by photo-fenton oxidation technology, Chemosphere 41 (2000) 1287–1294.
- [11] A.E. Papadopoulos, D. Fatta, M. Loizidou, Development and optimization of dark Fenton oxidation for the treatment of textile wastewaters with high organic load, J. Hazard. Mater. 146 (2007) 558–563.
- [12] Hyun-Seok Son, Jong-Kwon Im, Kyung-Duk Zoh, A Fenton-like degradation mechanism for 1,4-dioxane using zero-valent iron (Fe<sup>0</sup>) and UV light, Water Res. 43 (2009) 1457–1463.
- [13] J.A. Bergendahl, T.P. Thies, Fenton's oxidation of MTBE with zero-valent iron, Water Res. 38 (2004) 327–334.

- [14] L. Gomathi Devi, K.E. Rajashekhar, K.S. Anantha Raju, S. Girish Kumar, Kinetic modeling based on the non-linear regression analysis for the degradation of Alizarin Red S by advanced photo Fenton process using zero valent metallic iron as the catalyst, J. Mol. Catal. A: Chem. 314 (2009) 88–94.
- [15] A. Ghauch, Rapid removal of flutriafol in water by zero-valent iron powder, Chemosphere 71 (2008) 816–826.
- [16] M.A. Tarr, Chemical Degradation Methods for Wastes and Pollutants Environmental and Industrial Applications, Marcel Dekker Inc., New York, USA, 2003.
- [17] I. Grčić, D. Vujević, N. Koprivanac, Modeling the mineralization and discoloration in colored systems by (US)Fe<sup>2+</sup>/H<sub>2</sub>O<sub>2</sub>/S<sub>2</sub>O<sub>8</sub><sup>2-</sup> processes: A proposed degradation pathway, Chem. Eng. J. 157 (2010) 35–44.
- [18] T. Zhou, X. Lu, J. Wang, F.-S. Wong, Y. Li, Rapid decolorization and mineralization of simulated textile wastewater in a heterogeneous Fenton like system with/ without external energy, J. Hazard. Mater 165 (2009) 193–199.
- [19] Yang He, Jing-Feng Gao, Fang-Qing Feng, Cheng Liu, Yong-Zhen Peng, Shu-Ying Wang, The comparative study on the rapid decolorization of azo, anthraquinone and triphenylmethane dyes by zero-valent iron, Chem. Eng. J. in press. doi:10.1016/j.cej.2011.05.107.
- [20] T. Satapanajaru, C. Chompuchan, P. Suntornchot, P. Pengthamkeerati, Enhancing decolorization of Reactive Black 5 and Reactive Red 198 during nano zerovalent iron treatment, Desalination 266 (2011) 218–230.
- [21] L.G. Devi, S.G. Kumar, K.M. Reddy, C. Munikrishnappa, Effect of various inorganic anions on the degradation of Congo Red, a di azo dye, by the photoassisted fenton process using zero-valent metallic iron as a catalyst, Desalin. Water Treat. 4 (2009) 294–305.
- [22] L.G. Devi, K.S.A. Raju, S.G. Kumar, K.E. Rajashekhar, Photo-degradation of di azo dye Bismarck Brown by advanced photo-Fenton process: influence of inorganic anions and evaluation of recycling efficiency of iron powder, J. Taiwan Inst. Chem. E. 42 (2011) 341–349.
- [23] Y. Wu, S. Zhou, F. Qin, K. Zheng, X. Ye, Modeling the oxidation kinetics of Fenton's process on the degradation of humic acid, J. Hazard. Mater. 179 (2010) 533–539.

- [24] J.A. Cornell, Experiments and Mixtures, Designs Models and the Analysis of Mixture Data, second ed., J. Wiley and Sons, New York, 1990.
- [25] R.O. Rahn, M.I. Stefan, J.R. Bolton, E. Goren, P.S. Shaw, K.R. Lykke, Quantum Yield of the Iodide-Iodate Chemical Actinometer; dependence on wave length and concentrations, Photochem. Photobiol. 78 (2003) 146–152.
- [26] C. Dominguez, J. Garcia, M.A. Pedraz, A. Torres, M.A. Galán, Photocatalytic oxidation of organic pollutants in water, Catal. Today 40 (1998) 85–101.
- [27] I. Grčić, M. Obradović, D. Vujević, N. Koprivanac, Sono-Fenton oxidation of formic acid/formate ions in an aqueous solution: From an experimental design to the mechanistic modeling, Chem. Eng. J. 164 (2010) 196–207.
- [28] Y.H. Huang, T.C. Zhang, Effects of dissolved oxygen on formation of corrosion products and concomitant oxygen and nitrate reduction in zerovalent iron systems with or without aqueous Fe<sup>2+</sup>, Water Res. 39 (2005) 1751–1760.
- [29] S. Jaganathan, H. Vahedi Tafreshi, B. Pourdeyhimi, Modeling liquid porosimetry in modeled and imaged 3-D fibrous microstructures, J. Colloid Interface Sci. 326 (2008) 166–175.
- [30] M.H. Zahir, T. Suzuki, Y. Fujishiro, M. Awano, Perovskites with cotton-like morphology consisting of nanoparticles and nanorods: Their synthesis by the combustion method and their NO<sub>x</sub> adsorption behaviour, Appl. Catal. A: Gen. 361 (2009) 86–92.
- [31] I. Grčić, A. Šipić, N. Koprivanac, D. Vrsaljko, Global parameter of ultrasound exploitation (GPUE) in the reactors for wastewater treatment by sono-Fenton oxidation, Ultrason. Sonochem. 19 (2012) 270–279.
- [32] W.J. Cooper, C. Shao, D.R.S. Lean, A.S. Gordon, F.E. Scully Jr., Factors affecting the distribution of H<sub>2</sub>O<sub>2</sub> in surface waters, in: Environmental Chemistry of Lakes and Reservoirs, L.A. Baker, Washington D.C., 1994, pp. 390–422.
- [33] T. Oppenländer, Photochemical Purification of Water and Air, Wiley-VCH Verlag GmbH & Co. KGaA, Weinheim, 2003.
- [34] F.G. Kari, S. Hilger, S. Canonica, Determination of the reaction quantum yield for the photochemical degradation of Fe(III)EDTA – implications for the environmental fate of EDTA in surface waters, Environ. Sci. Technol. 29 (1995) 1008–1017